

Enhanced Fluid Dynamics in 3D Monolithic Reactors to Improve the Chemical Performance: Experimental and Numerical Investigation

Asuncion Quintanilla,* Gonzalo Vega, Pablo López, Francesca García, Enrique Madurga, Manuel Belmonte, and Jose A. Casas



Cite This: *Ind. Eng. Chem. Res.* 2021, 60, 14701–14712



Read Online

ACCESS |



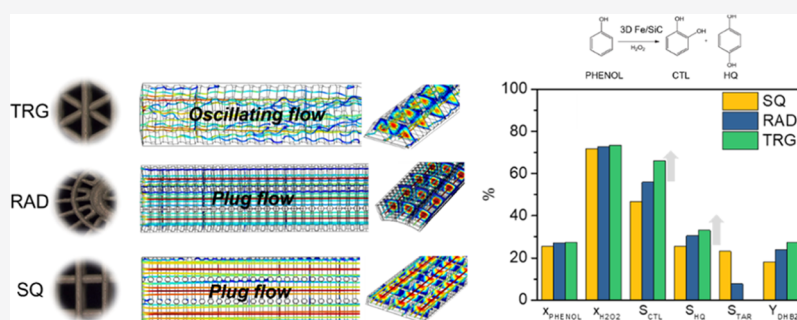
Metrics & More



Article Recommendations



Supporting Information



ABSTRACT: Three-dimensional (3D) Fe/SiC monoliths with parallel interconnected channels and different cell geometries (square, troncoconical, and triangular) were manufactured by robocasting and used as catalytic reactors in hydroxylation of phenol using hydrogen peroxide to produce dihydroxybenzenes; the reaction was performed at $C_{\text{phenol},0} = 0.33$ M, $C_{\text{phenol},0}:C_{\text{H}_2\text{O}_2,0} = 1:1$ M, $W_R = 3.7$ g, $T = 80\text{--}90$ °C, and $\tau = 0\text{--}254$ g_{cat}·h·L⁻¹ with water as a solvent. The values of the apparent kinetic rate constants demonstrated the superior performance of the triangular cell monoliths for hydrogen peroxide decomposition, phenol hydroxylation, and dihydroxybenzene production reactions. A computational fluid dynamic model was validated with the experimental results. It demonstrated that the triangular cell monoliths, with a lower channel hydraulic diameter and not-facing interconnections, provided a higher internal macrotortuosity that induced an oscillating flow of the liquid phase inside the channels, leading to an additional transverse flow between adjacent parallel channels. This behavior, not observed in the other two geometries, resulted in a better overall performance.

1. INTRODUCTION

One of the key factors that determine the reactor performance is the geometry of the reactor.^{1–3} It is designed to provide maximum conversion and selectivity at minimum catalyst load and operating cost. For this aim, the reactor must be adapted to achieve the best matching of fluid dynamics, heat transmission, and mass transport with the reaction kinetics.

The recent irruption of the additive manufacturing technologies, also known as three-dimensional (3D) printing technologies, in chemical engineering and related fields has opened new opportunities for the customized catalyst/reactor design, optimization of reaction performance, and process intensification.^{4–7} The unprecedented geometric freedom in design, with substantial precision and control, paced by the increasing availability of engineered materials (*i.e.*, polymers, ceramics, metals, and carbon-based materials) is extending the digital manufacturing not only to reactionware^{8–10} and microfluidic reactors^{11,12} but also to nonconventional catalyst carriers and structured packings.^{13,14}

In particular, a rising number of publications explore the rational design and preparation of 3D monolithic catalytic

systems with nonconventional geometries.^{15–30} The most common ones are the honeycomb monoliths with interconnected straight channels^{15,16,19,20,23,27} and also cross-channel structures.^{28,29} More complex ones are honeycomb monoliths with asymmetrical channels either by a progressive decrease in the channel section along the monolith²¹ or by alternating wide and narrow channels.²⁶ In addition, parallel channels with new cell morphologies, *i.e.* diamonds, stars, waves, etc.,²² and most disrupted like monoliths with a completely different internal periodic structure, such as tetrakaidecahedron, tetrahedron, cylinders,¹⁷ or diamonds,²⁵ have been successfully fabricated.

Received: August 1, 2021

Revised: September 26, 2021

Accepted: September 29, 2021

Published: October 8, 2021



Table 1. Physical Properties of Robocast Monoliths after Thermal Treatment^a

geometry	ρ_{geo} (g cm ⁻³)	ρ_{bulk}^b (g cm ⁻³)	ϵ_{total} (%)	ϵ_{wall} (%)	η (cells per cm ²)	δ_{wall} (μ m)	d_{H}^c (mm)	a_v (mm ⁻¹)
TRG	0.60	1.13	65	18	71	317	0.53	22.1
RAD	0.53	0.96	57	13	48	289	0.88–1	23.1
SQ	0.60	1.05	59	16	49	298	0.88	26.4

^aGeometrical and bulk densities (ρ_{geo} , ρ_{bulk}), open total and rod porosities (ϵ_{total} , ϵ_{wall}), cell density (η), wall channel thickness (δ_{wall}), hydraulic diameter (d_{H}), and channel interface area (a_v) of robocast monoliths used in reactions. ^b ρ_{bulk} refers to the wall volume, equivalent to the particle density in pellets. ^cCalculated as $4aP^{-1}$ (where a is the open channel area and P is the wetted perimeter).

These 3D-printed monoliths provided an upgrading performance compared to those manufactured by the conventional direct extrusion process or pelletized catalysts. For instance, Cesarano's group,¹⁵ pioneers in the development of the robocasting, a direct ink writing technique, reported better conversions in the catalytic combustion of a methane reaction upon interconnected channeled hexa-aluminate monoliths. Davó-Qijñonero et al.²¹ manufactured asymmetrical CuO/CeO honeycomb monoliths obtained from a 3D-printed polymeric template that were used in CO oxidation. These authors obtained higher reaction rates and CO conversions compared to the symmetrical monoliths. Wei et al.²² observed different product distribution in the Fischer–Tropsch reaction depending on the cell morphology of metal monoliths manufactured by selective laser sintering. Li et al.¹⁷ demonstrated a higher catalytic performance of the tetrahedron-type monoliths in the syngas methanation for methanol production upon 3D Ni–Al₂O₃/C monoliths prepared from a 3D polymeric template. In particular, higher CO conversion and selectivity to CH₄ were obtained in the 3D monoliths along with a lower pressure drop and temperature gradient compared to the powder Ni–Al₂O₃/C catalyst. Hajimirzaee et al.³⁰ prepared 3D cordierite monoliths where the geometry of the cells was modified by selecting different rotation angles between adjacent layers. These architectures with immobilized Pd/Pt were used as catalytic converters and tested in the oxidation of methane. The activity of the 3D converters was always superior to that provided by the conventional one, though there was not a clear superior architecture.

These studies agree about the beneficial impact that novel geometries have on fluid–solid contact. The macrochannel tortuosity created inside the monoliths promotes the turbulence in the flow stream, typically a gas phase, which results in an enhanced reactant and product mass transfer from the bulk gas to the catalyst wall, as well as a favored heat release.^{6,17,27,30,31} This reason has motivated the development of numerous works related to the numerical simulations of the gas flow inside the 3D monoliths to confirm the advantages of the novel designs.^{3,6,25,26,30,31}

Just few studies about computational fluid dynamics (CFD) applied to the 3D-printed monoliths are focused on the visualization of the gas flow in the inner geometry and the calculations of pressure drops and temperature distribution in one channel or the complete monolithic architecture. The present study goes one-step ahead by including the kinetic equations in the numerical computation software and thus, enables the multiphasic modeling of 3D customized monolithic catalytic systems.

Based on our recent works,^{27,32} 3D Fe/SiC honeycomb monoliths with interconnected channels were additive manufactured by robocasting with different inner morphologies and applied to a demanding liquid-phase reaction, the selective oxidation of hydrocarbons. A kinetic study was carried

out for the reaction modeling, and then a 3D computational fluid dynamic model was created considering the conservation of mass, momentum, and species together with chemical reactions. Afterward, the model was validated against the experimental results. In this way, the functional understanding of 3D-printed reactors with nonconventional architectures will be acquired based on the reactor geometrical aspects. Therefore, the results of this work will illustrate the full potential of coupling the 3D printing technology and numerical methods for the chemical reactor design.

2. MATERIALS AND METHODS

2.1. Three-Dimensional (3D)-Printed Fe/SiC Monoliths. Cylindrical monoliths with a ~ 14 mm diameter and a ~ 15 mm height were computer-aided designed in RoboCAD 4.0 (3-D Inks LLC) with different complex architectures (*i.e.*, cell geometry, cell density, and interconnected channel pattern) and printed with a three-axis robocasting system (A-3200, 3-D Inks LLC) at room temperature. The details of the Fe/SiC ink formulation, 3D periodic lattice designed, printing process, and final consolidation by means of thermal treatments are described elsewhere.²⁷

Table 1 summarizes the main physical characteristics of the 3D-printed monoliths with the three selected architectures: troncoconical (RAD), triangular (TRG), and square (SQ) cells, and Figure 1 shows some photographs of these structures. The digital source designs are provided in Figure S1 of the Supporting Information (SI). The characteristic length values of the cells, given in Figure 1a, ranged from 0.86 to 0.96 mm, depending on the geometry.

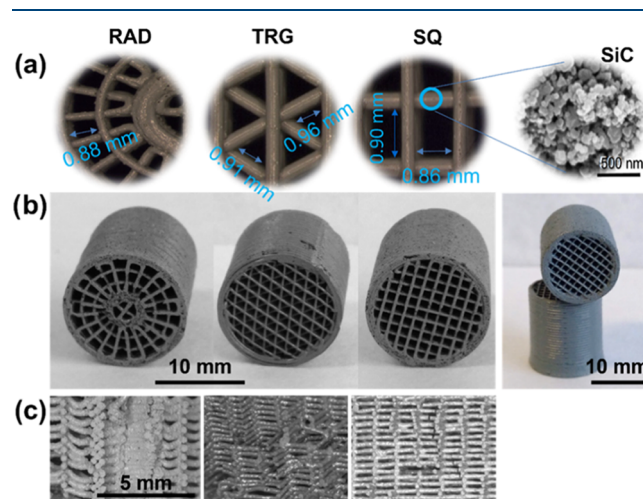


Figure 1. Cell-side optical views (a), 3D cylindrical Fe/SiC structures after the thermal treatment (b), and cross-sectional optical views (c) of the honeycomb monoliths with troncoconical (RAD), triangular (TRG), and square (SQ) cells.

According to these values and the geometry, the hydraulic diameter (d_H) was calculated and, as shown in Table 1, varied from 0.88 to 1.00 mm for RAD and was kept constant with 0.52 mm for TRG and 0.88 mm for SQ cells. Thus, 3D cylindrical monoliths, with the same external dimensions ($\sim 14 \times 15$ mm) but different d_H s exhibit different cell densities (η), being particularly high for the TRG ($\eta = 71$ cells per cm^2) with the lowest cell size, as shown in Figure 1b. In the three monoliths, the millichannels are parallel and laterally interconnected with a distinct spatial distribution depending on the design (see the cell-size photographs in Figure 1c and the schematic representations in Figure S1c of the SI). Accordingly, SQ cells contain fully facing lateral interconnections, while TRG cells present interconnections that are staggered located (or not-facing located), and RAD cells show an intermediate situation with two types of lateral interconnected channels, one of them fully facing that increases the area from the inner ring toward the outer ring, and another one (those in the center of the monolith) where the lateral interconnections are not completely facing. In the three geometries, the interconnections have the identical dimensions within each layer, which corresponds to the wall thickness ($\delta_{\text{wall}} \sim 300 \mu\text{m}$).

On the other hand, the 3D monoliths present quite similar densities and porosities (see Table 1), though some dimensional differences mainly in the wall thickness were observed due to the shrinking of the pieces during the thermal treatment (at 600 °C in air for 2 h and then at 1200 °C in an argon atmosphere for 5 min in a pressureless spark plasma sintering furnace, SPS-510CE; Fuji Electronic Industrial Co., Ltd). η is the most distinct characteristic, which depends on the cell geometry and d_H . Further details on geometrical characterization of the monolith samples can be found elsewhere.²⁷

The Fe content remained invariable for all monoliths, i.e. 0.52 ± 0.03 wt %, as well as the specific surface area ($S_{\text{BET}} = 39 \text{ m}^2 \text{ g}^{-1}$). Regarding the active catalytic phase, iron silicides, viz. Fe_3Si and $\alpha\text{-FeSi}_2$, identified by Mössbauer spectroscopy, are considered as the iron catalytic species.²⁷

2.2. Kinetic Study of Phenol Hydroxylation. The kinetic model discriminated for TRG monoliths in our previous work³² is as follows

$$(-r_{\text{H}_2\text{O}_2}) = \frac{k_{\text{H}_2\text{O}_2} C_{\text{H}_2\text{O}_2}}{1 + K C_{\text{H}_2\text{O}_2}} \quad (1)$$

$$(-r_{\text{phenol}}) = \frac{k_{\text{phenol}} C_{\text{phenol}} C_{\text{H}_2\text{O}_2}}{1 + K C_{\text{H}_2\text{O}_2}} \quad (2)$$

$$r_{\text{CTL}} = \frac{k_{\text{CTL}} C_{\text{phenol}} C_{\text{H}_2\text{O}_2}}{1 + K C_{\text{H}_2\text{O}_2}} \quad (3)$$

$$r_{\text{HQ}} = \frac{k_{\text{HQ}} C_{\text{phenol}} C_{\text{H}_2\text{O}_2}}{1 + K C_{\text{H}_2\text{O}_2}} \quad (4)$$

The reaction rates are expressed in $\text{mol g}_{\text{CAT}}^{-1} \text{h}^{-1}$ and concentrations (C_i) in mol L^{-1} . As can be seen, the H_2O_2 decomposition occurs according to the Langmuir–Hinshelwood–Hougen–Watson kinetic model (eq 1), while the phenol hydroxylation (eq 2), as well as catechol (CTL, eq 3) and hydroquinone (HQ, eq 4) occurs according production, to an Eley–Rideal kinetic model. This means that H_2O_2 molecules are adsorbed on the iron active sites and

decomposed into the hydroxyl radical species (HO^\bullet), which react with phenol in solution leading to the DHBZ formation. The phenol hydroxylation occurs until complete consumption of the H_2O_2 oxidant.³²

The kinetic model, eqs 1–4, was obtained in the absence of external and internal mass transfer limitation according to the Carberry number and Weisz–Prater modulus calculated at the different operating conditions, respectively. However, the kinetic rate constants (viz. $k_{\text{H}_2\text{O}_2}$, k_{phenol} , k_{CTL} , and k_{HQ}) were considered apparent because, though it is not a diffusion-controlled process, they lumped ratios of constants of the elemental steps mechanistically involved.³²

Herein, the apparent kinetic rate constants for the SQ and RAD monoliths were calculated from the corresponding experimental data (C_i) vs space time ($\tau = W \cdot Q_L^{-1}$) profiles. For that, the same experimental setup, operating conditions, and experimental proceeding as for the TRG monoliths were employed.³² Briefly, the reactor was constituted by three stacked monoliths (total catalyst weight, $W_R \sim 3.7$ g) and was operated at $C_{\text{phenol},0} = 0.33$ M, $C_{\text{phenol},0} : C_{\text{H}_2\text{O}_2,0} = 1:1$ M, $T = 80, 85$ and 90 °C, $\tau = 0\text{--}254 \text{ g}_{\text{cat}} \cdot \text{h} \cdot \text{L}^{-1}$ (or flow rate, Q_L , $0\text{--}0.25 \text{ mL min}^{-1}$) and with water as a unique solvent. The elucidated kinetic equations were considered for the CFD mathematical modeling.

A preliminary set of runs were carried out to measure the temperature inside the reactor at different axial and radial positions of the monolithic bed and at different operating conditions (i.e., $Q_L = 0.25$ and 2 mL min^{-1} , and $T_{\text{heating fluid}} = 85\text{--}95$ °C), using a digital thermocouple (TENMA 72-7712). A temperature gradient less than 0.5 °C between the center and the wall of the reactor was measured only at the highest flow rate of 2 mL min^{-1} , being negligible at 0.25 mL min^{-1} . According to the results, the reactor operates under isothermal conditions.

On the other hand, the conversion (X) of reactants (denoted by j : phenol or H_2O_2), phenol selectivity (S), and yield (Y) to the identified products (n : CTL, HQ, resorcinol (RSL), or p -benzoquinone (BQ)) were calculated as follows:

$$X_j(\%) = \frac{C_{j,0} - C_{j,t}}{C_{j,0}} \times 100 \quad (5)$$

$$S_n(\%) = \frac{C_n}{C_{\text{phenol},0} \cdot X_{\text{phenol}}} \times 100 \quad (6)$$

$$Y_n(\%) = S_n \cdot X_{\text{phenol}} \times 100 \quad (7)$$

All of the concentrations (C) are expressed on mole basis. The subscripts 0 and t stand for the initial and a given reaction time, respectively.

2.3. Analytical Methods. The progress of the reaction was followed by taking liquid samples periodically from the reactor outlet. The steady state was reached after 2–8 h, depending on the space time. Phenol and the aromatic byproducts, viz. HQ, CTL, BQ, and RSL, were determined by high-performance liquid chromatography (Ultimate 3000, Thermo Scientific, C18 $5 \mu\text{m}$ column 150×4.6 mm, 4 mM H_2SO_4 as a mobile phase, DAD detector at wavelengths of 210, 246, and 246 nm). The H_2O_2 concentration was measured using the TiOSO_4 method in a Cary 60 UV–Vis spectrophotometer.³³

2.4. CFD Modeling with COMSOL Multiphysics. A numerical approach using CFD is applied to predict the effect

of the architecture or geometrical aspects of the 3D-printed monoliths on the fluid dynamics, pressure drop, and reactant conversion. Software COMSOL Multiphysics v5.5 (COMSOL Inc., Burlington, MA) was used to perform the 3D multiscale modeling. This commercial software is based on the finite element method for the discretization of the domains to solve the model equations.

2.4.1. Geometry. For the fluid dynamic study, three consecutive 3D channels were built to study the transverse flow by the interconnections, while for the modeling study (that coupling the species transport and reaction kinetics to the fluid dynamic analysis), only one 3D channel was considered for simplification. In this latter case, half of the channels for SQ and RAD monoliths were used and the symmetry applied; such symmetry could not be considered in the TRG geometry, as deduced by the fluid dynamic study. The geometries digitally designed in CAD and exported to COMSOL Multiphysics v5.5 are provided in Figure S2 of the SI. To simulate the reactor performance, the channel dimensions were identical to the 3D-printed samples used in the reaction (*i.e.*, open channel width, wall thickness, angles between filaments) and the length corresponded to that of the reactor (*ca.* 44 mm, according to the three stacked monoliths used). These dimensions are also included in Figure S2 of the SI.

2.4.2. Initial Considerations. The proposed CFD model was based on the following considerations:

- Flow regime: the lineal velocities in the channel are very low, which implies that the Reynolds number (Re) is less than 1. For instance, at 2 mL min⁻¹ in the TRG geometry ($d_H = 0.53$ mm), the velocity is 2.33×10^{-4} m s⁻¹ and $Re = 0.37$. Therefore, the Stokes flow or creeping flow has been used.
- Fluid-phase properties: according to the initial reactant concentration ($C_{phenol,0} = C_{H_2O_2,0} = 0.33$ M) in the liquid phase, the major species is water. Therefore, the transport of diluted species can be considered to model the reactant transport in the liquid phase by COMSOL, and the physical properties of the reaction medium are those corresponding to water under the operating conditions studied ($P = 1$ atm and $T = 80$ – 90 °C).
- Monolithic material: the wall is mainly made of SiC (the Fe amount is very low). Therefore, the channel wall can be considered to be isotropic. The internal pore diffusion of the reactant is produced by the effective diffusion, considering a tortuosity model, which will be further described in eqs 12 and 13.
- Heat transfer: the process experimentally takes place in an isothermal regime. Then, the heat transfer would not have an appreciable effect on the catalytic performance and, consequently, it has not been considering in this study.

2.4.3. Governing Equations and Boundary Conditions. The governing equation for the liquid mass balance at the steady state is

$$\rho \nabla \cdot (\mathbf{u}) = 0 \quad (8)$$

where ρ is the mass density and \mathbf{u} is the fluid velocity field calculated using the linear momentum balance equation (Navier–Stokes equation) with the inertial forces very small compared to the viscous forces (according to the governing creeping flow, and $Re < 1$)

$$0 = \nabla \cdot [-p\mathbf{I} + \mu(\nabla \mathbf{u} + (\nabla \mathbf{u})^T)] + \mathbf{F} \quad (9)$$

In this equation, μ (SI units: kg m⁻² s⁻¹) is the fluid viscosity, p (SI units: Pa) is the pressure, and \mathbf{F} is the identity tensor.

The abovementioned equations are complemented with the following boundary conditions:

- at the walls inside the monoliths, the no-slip condition is employed: $\mathbf{u} = 0$
- at the inlet of channels, the input velocity is calculated as a function of Q_L and the cross-sectional area (A), according to the expression

$$\mathbf{u} = -n \cdot \frac{Q_L}{A} \quad (10)$$

with n being the unit normal vector pointing outside the monolith boundary.

- at the outlet of channels, the atmospheric pressure is imposed: $p = p_0$
- symmetry $n \cdot \mathbf{u} = 0$

Equations 8 and 9 are coupled with convection-diffusion balance equation for the species i in the fluid along the channel

$$\nabla \cdot (-D_i \nabla c_i) + \mathbf{u} \cdot \nabla c_i = 0 \quad (11)$$

and the diffusion-reaction balance equation for the reactants inside the porous catalytic wall

$$\nabla \cdot (-D_{i,e} \nabla c_i) = R_i \quad (12)$$

where D (m² s⁻¹) is the diffusion coefficient of the species in the aqueous phase and D_e (m² s⁻¹) is the effective diffusion coefficient of the species in the porous wall. It is calculated from the molecular diffusion considering the properties of the porous media

$$D_{i,e} = D_i \cdot \frac{\varepsilon_{\text{wall}}}{\tau_{\text{wall}}} \quad (13)$$

$\varepsilon_{\text{wall}}$ is the rod porosity for each architecture, the values are provided in Table 1, and the wall tortuosity (τ_{wall}) is set as 1.2 typical for monolithic catalysts. R (mol m⁻³ s⁻¹) is the reaction rate, equal to eq 1 for H₂O₂ and (2) for phenol. Note that for unit consistency, the reaction rates of a catalytic system expressed in terms of kg of mass of catalyst will be multiplied by the bulk density (ρ_{bulk}) of the monolith (see Table 1), which is the spatial domain where the chemical reaction occurs.

The boundary conditions for the mass balance solutions of eqs 11 and 12 are as follows:

- at the walls, $n \cdot (-D \nabla c) + \mathbf{u} \cdot c = 0$
- at the inlet, $C_{phenol,0} = C_{H_2O_2,0} = 0.33$ M
- at the outlet, $n \cdot (-D \nabla c) = 0$

Finally, the 3D motions of particles settling in the Stokes flow were numerically tracked to visualize the passage of the flow between adjacent parallel channels through the interconnections. The particle tracking was described by the Newtonian, first-order formulation, and combined with the Navier–Stokes flow and resolved in a time-dependent study

$$\frac{d(m_p \cdot \mathbf{v})}{dt} = \mathbf{F}_i \quad (14)$$

where $\mathbf{v} = d\mathbf{q}/dt$; \mathbf{q} (m) is the particle position, m_p (kg) is the particle mass, and \mathbf{F} (N) is the total force on the particles. In

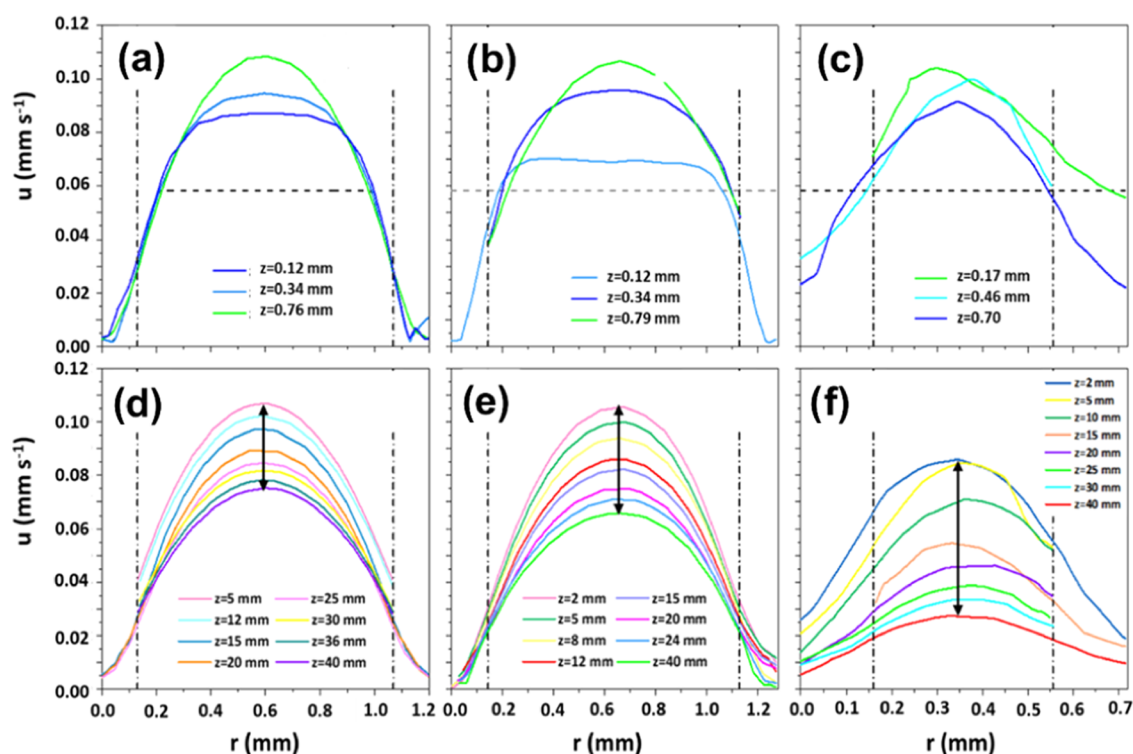


Figure 2. Radial velocity profiles for the different monolith morphologies: SQ (a, d), RAD (b, e), and TRG (c, f) at different axial positions (z) at $T = 85\text{ }^{\circ}\text{C}$ and $Q_L = 0.5\text{ mL min}^{-1}$.

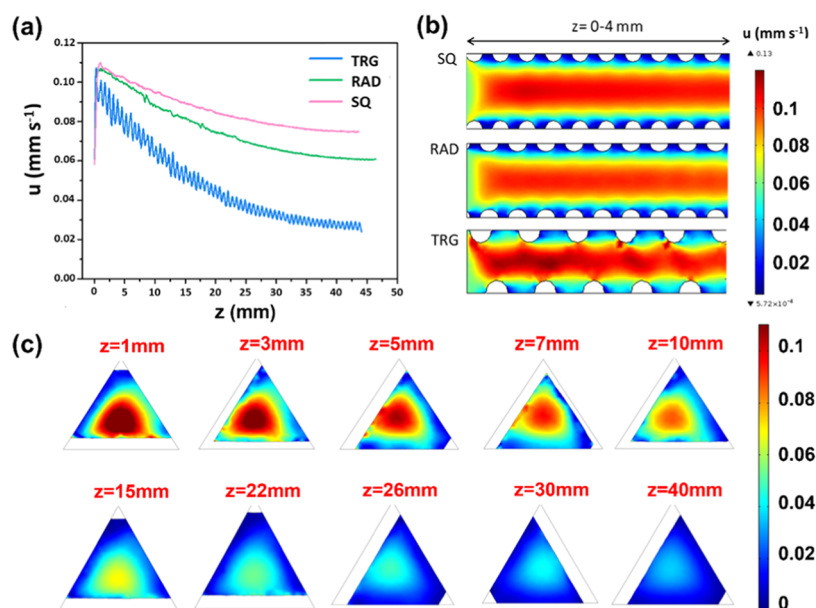


Figure 3. Axial velocity profiles (a) and 2D velocity profiles at the entrance of the channel (b) for the different monolith morphologies at $r = 0$, $T = 85\text{ }^{\circ}\text{C}$, and $Q_L = 0.5\text{ mL min}^{-1}$. Cross-sectional velocity plots along the TRG monolithic reactor at $T = 85\text{ }^{\circ}\text{C}$ and $Q_L = 0.5\text{ mL min}^{-1}$ (c).

this study, 50 specific particles, with a suitable diameter ($1\text{ }\mu\text{m}$) to be visible in the 3D animation, were released at the entrance of the liquid flow rate (0.5 mL min^{-1}), every 20 s. The particle density was equal to that of the water at room temperature.

2.4.4. Meshing. The spatial discretization of the 3D geometries in both domains, open channel and wall, was carried out by an unstructured mesh with tetrahedral elements. A mesh sensitivity analysis, with nine different meshes, was conducted for the TRG monolith (the most complex geometry) to acquire the optimum mesh size that will give a

good balance between accuracy and computational time. The results of this study are provided in Table S1 and Figure S3 of the SI. It was found that 1.01×10^6 tetrahedral elements were enough to obtain independent grid mesh results with the mentioned conditions. The same grid mesh was applied for RAD and SQ monoliths.

3. RESULT AND DISCUSSION

3.1. Fluid Dynamic Study. 3.1.1. Velocity Profiles. Figure 2 shows the radial velocity profiles of each geometry at

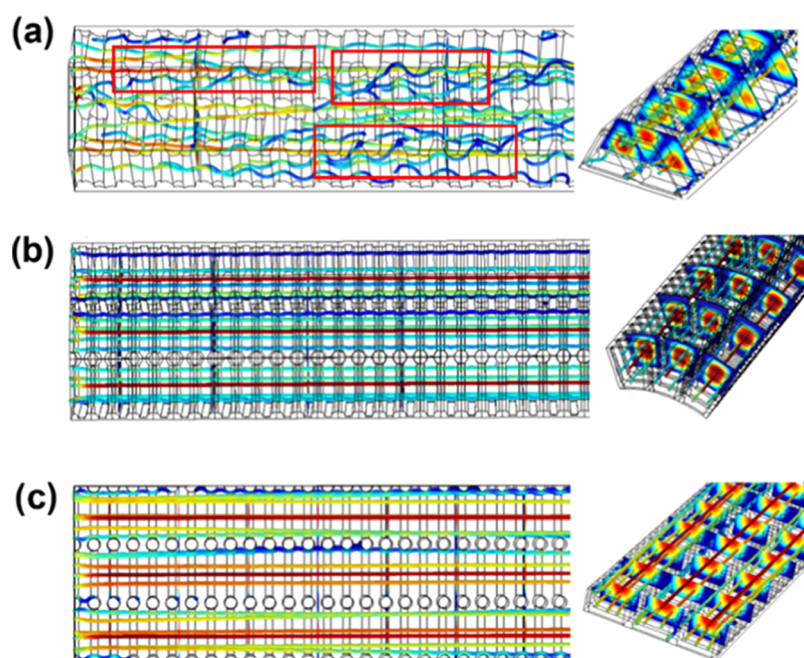


Figure 4. Velocity streamlines along the reactor in three consecutive interconnected channels for the different monolith morphologies: TRG (a), RAD (b), and SQ (c) at $T = 85\text{ }^{\circ}\text{C}$ and $Q_L = 0.5\text{ mL min}^{-1}$. The streamlines passing to the adjacent channel are highlighted in a red color (a). The videos of the dynamic simulations are provided in Table S2 of the Supporting Information.

different channel lengths (z). The horizontal dashed line represents the lineal velocity ($u_L \approx 0.058\text{ mm}\cdot\text{s}^{-1}$, calculated as the ratio between the flow rate and the monolith cross section), while the vertical lines indicate the position of the channel wall (or catalytic filament). The profiles present discontinuities when the selected x - y plane coincides with the wall, instead of an interconnection, and the velocity is zero. As can be seen, the flow completely develops before the first millimeter of the channel, so the effects caused by the entrance to the channel can be considered negligible. The velocity profile develops in a parabolic shape until it reaches a maximum, $u_{\max} \approx 0.11\text{ mm}\cdot\text{s}^{-1}$ at $z = 0.76\text{ mm}$ (SQ); $z = 0.79\text{ mm}$ (RAD) and $z = 0.17\text{ mm}$ (TRG), from which the velocity decreases as the fluid flows through the channel due to the fluid friction with the walls. It should be noted that this decrease is more notable in the TRG channels compared to the SQ and RAD. In addition, the maximum velocity in the TRG geometry oscillates with respect to the center of the channel, while for the other geometries, it is always located at the center (only with a slight deviation in the case of the RAD geometry).

These phenomena are better illustrated in Figure 3. The 2D axial velocity profiles (in a plane center of the channel) show that the reduction of the velocity with respect to the maximum reached ($u_{\max} \approx 0.11\text{ mm}\cdot\text{s}^{-1}$), once the flow is fully developed, is much more noticeable for the TRG channel (97%) compared to the RAD (44%) and SQ (30%). In addition, in the TRG geometry, the velocity values clearly fluctuate (Figure 3a). The fluid does not follow a straight path as for SQ and RAD but moves along colliding with the channel wall (Figure 3b), and this results in an oscillating flow (Figure 3c).

Therefore, the TRG cell geometry has a different fluid dynamic behavior than the SQ and RAD. This is mainly because the latter are manufactured by superimposing two layers of filaments so that the interconnections and the filaments face in a two-by-two manner. Instead, the TRG geometry is created by superimposing three layers of filaments

so the interconnections are staggered and do not face each other. As a result, the TRG geometry accounts for a higher macrochannel tortuosity that causes a deviation of the fluid in the channel.

Another important aspect related to the presence of the interconnections is the chance of inducing a liquid flow between adjacent channels, which seems more likely in the TRG geometry. To gain a deeper insight into this, particle tracking was carried out to observe the fluid path in three consecutive 3D channels. Figure 4 shows the resulting velocity streamlines in each 3D geometry. The videos obtained from the dynamic (temporal) simulation can be accessed from the SI (Table S2). As can be seen, the flow between the interconnections is an exclusive phenomenon of the TRG geometry channel, while for RAD and SQ geometries, the fluid follows a straight path in each channel and the interconnections do not have any significant effect on its fluid dynamics. Likewise, it was possible to statistically determine by the particle tracking study that 50% of the released particles in the TRG geometry leave the monolith in the same channel in which they began.

In conclusion, the oscillating flow induced by the high macrochannel tortuosity exhibited by the TRG monoliths due to the low cell sizes, high cell density, and, above all, not-facing channelled interconnections, promotes the transverse flow between adjacent parallel channels, the fact that, obviously, will prolong the contact time between the reactants and the catalytic monolith.

3.1.2. Pressure Drop. The calculated pressure drop (ΔP) values at the exit of the reactor are similar for the SQ and RAD channels and always lower than that obtained for TRG. The values are provided in Figure S4 of the SI. According to these results, the oscillatory flow along with the fluid passing from one channel to another through the interconnections produce a greater friction of the fluid with the walls and, therefore, a greater ΔP , increasing the energy requirements. However, for

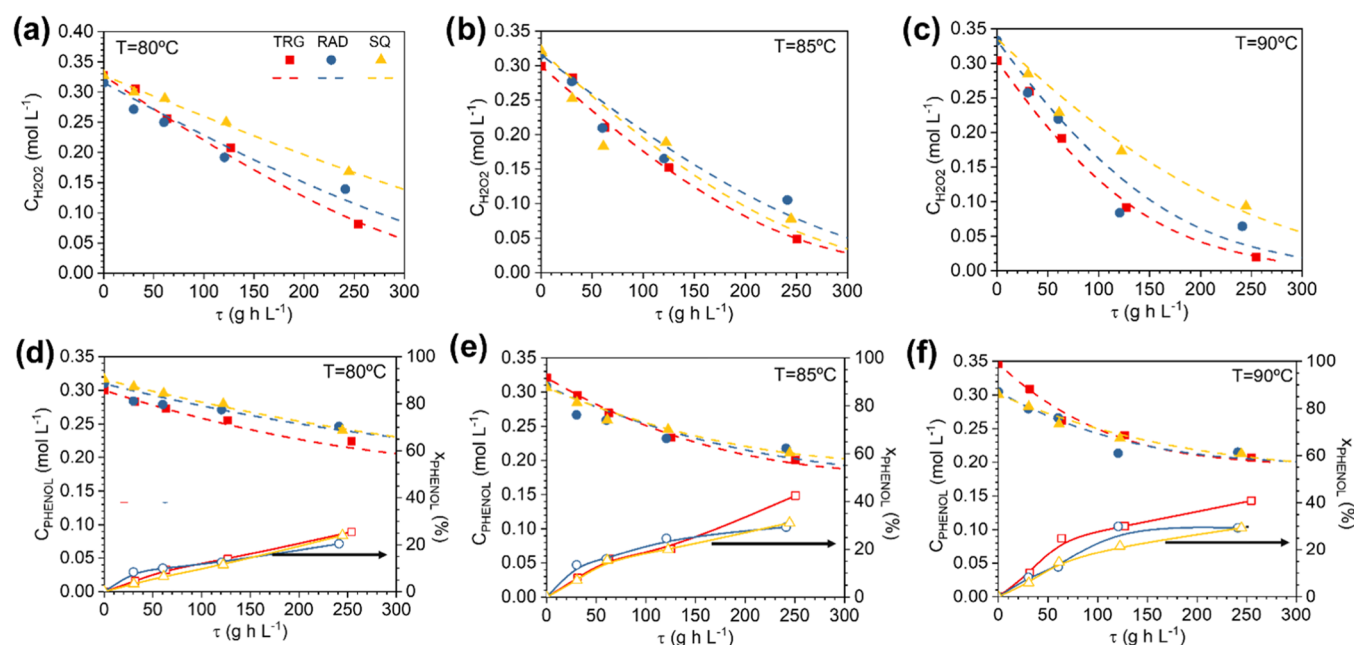


Figure 5. Experimental (symbols) and predicted (curves) time course of H_2O_2 (a–c) and phenol (d–f) for the different monolith morphologies and temperatures. Operating conditions are as follows: $C_{\text{phenol},0} = C_{\text{H}_2\text{O}_2,0} = 0.33 \text{ M}$, $W_R = 3.7 \text{ g}_{\text{CAT}}$, $T = 80\text{--}90^\circ\text{C}$, and $\tau = 0\text{--}254 \text{ g}_{\text{cat}}\cdot\text{h L}^{-1}$.

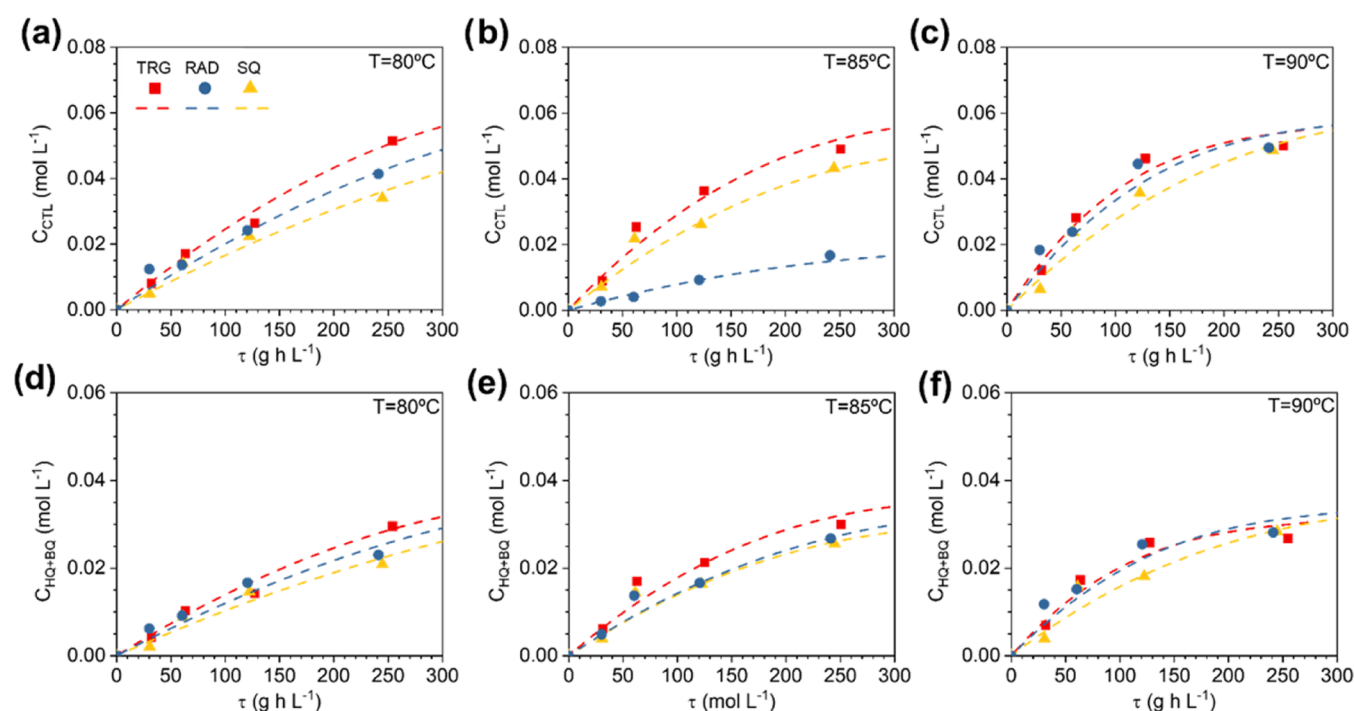


Figure 6. Experimental (symbols) and predicted (curves) time course of catechol (a–c) and hydroquinone (d–f) for the different monolith morphologies and temperatures. Operating conditions are as follows: $C_{\text{phenol},0} = C_{\text{H}_2\text{O}_2,0} = 0.33 \text{ M}$, $W_R = 3.7 \text{ g}_{\text{CAT}}$, $T = 80\text{--}85^\circ\text{C}$, and $\tau = 0\text{--}254 \text{ g}_{\text{cat}}\cdot\text{h L}^{-1}$.

the worst case (TRG geometry, $Q = 2 \text{ mL min}^{-1}$ and $T = 80^\circ\text{C}$), the maximum pressure drop is 81.9 mPa, a negligible value compared to the working pressure (101.3 kPa). Therefore, it can be concluded that the pressure drop will not be a limiting factor.

3.2. Catalytic Performance and Kinetic Results. The results obtained in the experimental investigation to evaluate the effect of the inner morphology of the monoliths in the

reaction performance at the different temperatures are shown in Figures 5 and 6.

Regarding the H_2O_2 and phenol concentration profiles (Figure 5), measured at the reactor exit, they slightly differ from one morphology to another, though TRG seems to be the most favorable for the H_2O_2 decomposition, in particular at 90°C (Figure 5c). Accordingly, phenol conversion is also particularly enhanced at that temperature ($X_{\text{PHENOL}} = 42\%$ for TRG vs $\sim 35\%$ for SQ and RAD, see Figure 5f). On the

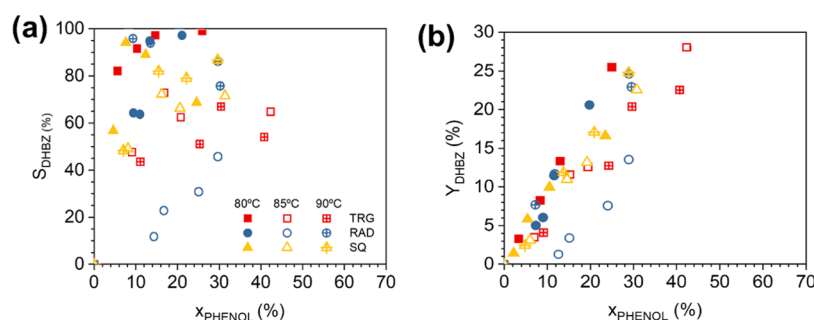


Figure 7. DHBZ selectivity (a) and yield (b) vs phenol conversion for the different monolith morphologies and temperatures. Operating conditions are as follows: $C_{\text{phenol},0} = C_{\text{H}_2\text{O}_2,0} = 0.33 \text{ M}$, $W_R = 3.7 \text{ g}_{\text{CAT}}$, $T = 80\text{--}90 \text{ }^\circ\text{C}$, and $\tau = 0\text{--}254 \text{ g}_{\text{cat}}\cdot\text{h}\cdot\text{L}^{-1}$.

contrary, the product distribution is most significantly affected by the cell geometry, and DHBZ is preferentially produced with a TRG morphology (Figure 6a–c), in reduction of the BQ and tar species.²⁷

The most appropriate reaction temperature for the phenol hydroxylation is $80 \text{ }^\circ\text{C}$ to avoid the overoxidation of DHBZ and to maintain a selectivity above 90% for all of the morphologies, as shown in Figure 7a. Note that TRG provides the highest DHBZ selectivity, as high as 99% at $80 \text{ }^\circ\text{C}$, whereas this value is 92% for SQ and 97% for RAD. The ratio HQ:CTL is usually maintained at 1.8 M. Most significant is the DHBZ yield achieved, $Y_{\text{DHBZ}} = 27\%$ for TRG at $85 \text{ }^\circ\text{C}$ in contrast to 24% for SQ and RAD at $90 \text{ }^\circ\text{C}$, as shown in Figure 7b.

According to this, the inner morphology of the monoliths influences the reactor performance for liquid-phase reactions such as the hydroxylation of phenol with H_2O_2 . In this case, the H_2O_2 conversion, the DHBZ selectivity, and yield are more affected than the phenol conversion, and the TRG morphology seems to be superior. This occurs despite its lower interface area (a_v in Table 1) compared to SQ and RAD. Therefore, other factors play a role, in particular, a better contact between reactants and the Fe/SiC catalyst induced by the oscillating flow. The collision of the reactants to the catalytic wall contributes to enhancing the radial mass transport. This may favor the production of the surface HO^\bullet radical species, and at high temperatures, when HO^\bullet surface reactive desorption is more favored, also the phenol hydroxylation. Another important factor could be the more prolonged contact of the reactants inside the monoliths due to the transverse flow between adjacent parallel channels and the significant slowing down velocity along the channel due to the higher friction of the liquid with the catalytic wall. This implies to operate at higher space times than those corresponding to the flow rate used. Note that longer space times do not provoke the overoxidation of the DHBZ but a better efficiency in the consumption of the HO^\bullet species. Finally, the slightly higher accessibility to the Fe sites, due to the higher wall porosity and wall thickness of the TRG morphology (see Table 1), also plays an important role.

For the gas-phase reactions previously studied,^{6,17,30,31} the enhanced reactant and product mass transfer from the bulk gas to the catalyst wall were provided as the main reasons, as well as favored the heat release. In this work, the abovementioned factors will be further analyzed based on the CFD modeling of the interconnected monolithic reactors. To this aim, the kinetic modeling for the mathematical description of the course of the reaction is necessary and, therefore, the apparent kinetic rate equations have been obtained for each geometry.

The fitting of the discriminated kinetic model for the TRG monoliths in our previous work,³² eqs 1–4, to the experimental concentration profiles obtained for SQ and RAD allowed the calculation of the apparent kinetic rate constants (*viz.* $k_{\text{H}_2\text{O}_2}$, k_{phenol} , k_{CTL} , and k_{HQ}) collected in Table 2

Table 2. Apparent Kinetic Parameter Values for Phenol Hydroxylation by H_2O_2 over 3D Fe/SiC Honeycomb Monoliths with Different Morphologies at Different Temperatures^a

T (°C)	Geometry	$k_{\text{H}_2\text{O}_2}$ ($\text{L h}^{-1} \text{ g}_{\text{CAT}}^{-1}$)	k_{PHENOL} ($\text{L}^2 \text{ mol}^{-1} \text{ h}^{-1} \text{ g}_{\text{CAT}}^{-1}$)	k_{CTL}	k_{HQ}
		$\frac{k_{\text{H}_2\text{O}_2} C_{\text{H}_2\text{O}_2}}{1 + 11.84 C_{\text{H}_2\text{O}_2}}$	$\frac{k_i C_{\text{PHENOL}} C_{\text{H}_2\text{O}_2}}{1 + 11.84 C_{\text{H}_2\text{O}_2}}$		
80	TRG	$1.66 \cdot 10^{-2}$	$2.31 \cdot 10^{-2}$	$1.37 \cdot 10^{-2}$	$7.78 \cdot 10^{-3}$
	RAD	$1.35 \cdot 10^{-2}$	$1.75 \cdot 10^{-2}$	$1.07 \cdot 10^{-2}$	$6.39 \cdot 10^{-3}$
	SQ	$1.03 \cdot 10^{-2}$	$1.73 \cdot 10^{-2}$	$8.50 \cdot 10^{-3}$	$5.28 \cdot 10^{-3}$
85	TRG	$1.54 \cdot 10^{-2}$	$3.05 \cdot 10^{-2}$	$1.27 \cdot 10^{-2}$	$7.81 \cdot 10^{-3}$
	RAD	$1.33 \cdot 10^{-2}$	$2.36 \cdot 10^{-2}$	$3.39 \cdot 10^{-3}$	$6.13 \cdot 10^{-3}$
	SQ	$1.50 \cdot 10^{-2}$	$2.22 \cdot 10^{-2}$	$9.90 \cdot 10^{-3}$	$6.03 \cdot 10^{-3}$
90	TRG	$1.50 \cdot 10^{-2}$	$2.85 \cdot 10^{-2}$	$1.07 \cdot 10^{-2}$	$5.94 \cdot 10^{-3}$
	RAD	$1.37 \cdot 10^{-2}$	$1.81 \cdot 10^{-2}$	$9.79 \cdot 10^{-3}$	$5.68 \cdot 10^{-3}$
	SQ	$9.60 \cdot 10^{-3}$	$1.39 \cdot 10^{-2}$	$7.58 \cdot 10^{-3}$	$4.34 \cdot 10^{-3}$

^aRates in $\text{mol g}_{\text{CAT}}^{-1} \text{ h}^{-1}$ and concentrations in mol L^{-1} .

for the three temperatures and morphologies. The kinetic parameter (K) that includes the H_2O_2 adsorption constant was maintained with the same value as that estimated for TRG since the catalytic material is identical (*i.e.* Fe load, S_{BET} and similar ϵ_{wall}). Note that the apparent kinetic rate constant values are always higher for TRG monoliths at a given reaction temperature (see Table 2 and Figure S5 of the SI where the data are included in bars for the sake of comparison), which highlights their superior performance.

The validation of the kinetic model for phenol, H_2O_2 , and DHBZ can be confirmed, as illustrated in Figures 5 and 6 by the good coincidence between the experimental (in symbols) and predicted (in lines) concentration profiles. Typically,

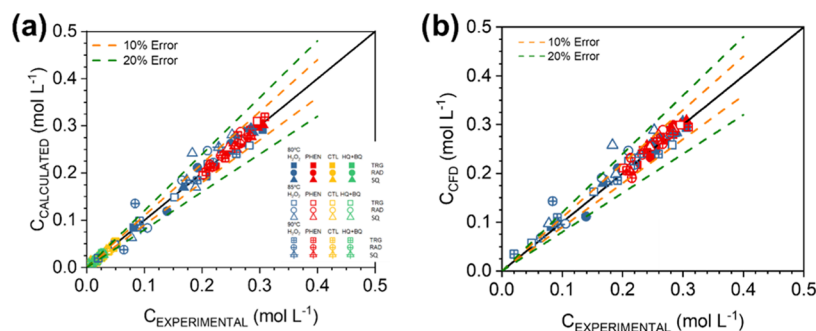


Figure 8. Parity plot of experimental and calculated concentrations by the kinetic equations (a) and by the CFD simulation (b) for the different monolith morphologies. Operating conditions are as follows: $C_{\text{phenol},0} = C_{\text{H}_2\text{O}_2,0} = 0.33 \text{ M}$, $W_R = 3.7 \text{ g}_{\text{CAT}}$, $T = 80\text{--}90 \text{ }^\circ\text{C}$, and $\tau = 0\text{--}254 \text{ g}_{\text{cat}}\cdot\text{h}\cdot\text{L}^{-1}$.

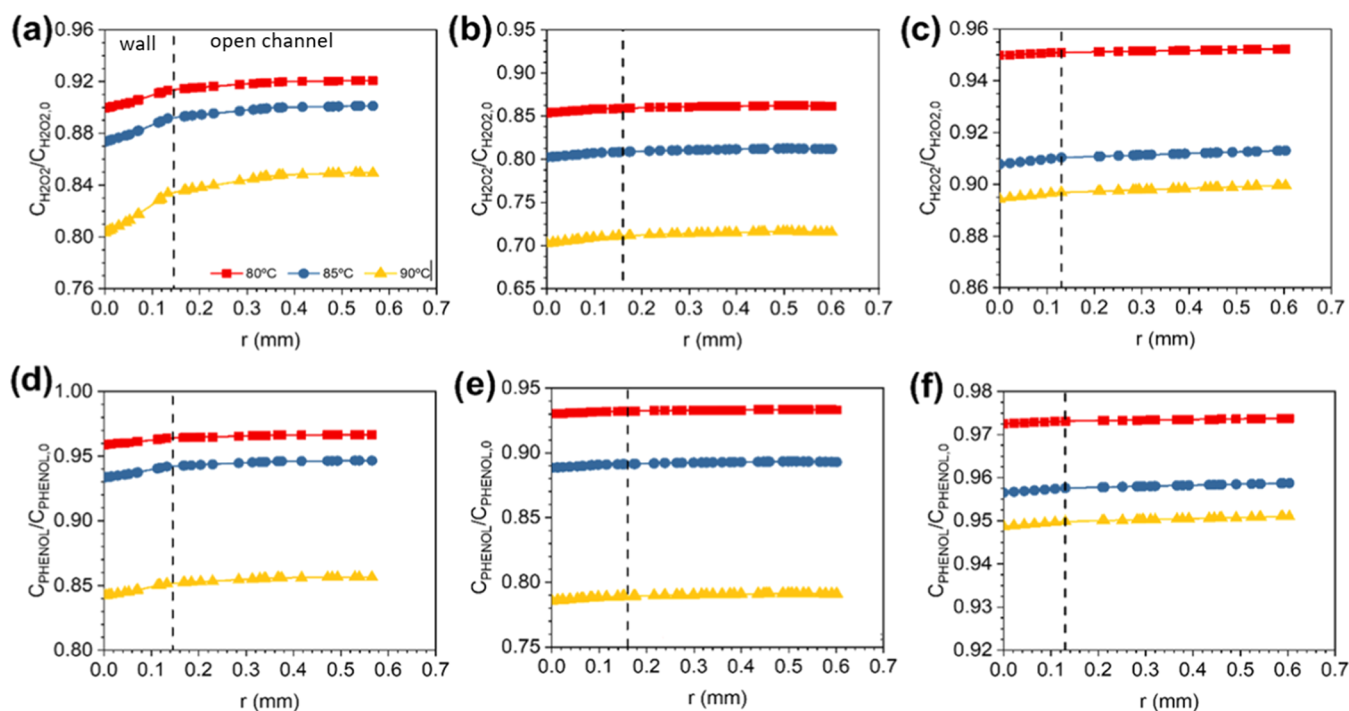


Figure 9. Radial concentration profiles of H_2O_2 (a–c) and phenol (d–f) for the different monolith morphologies: RAD (a, d), TRG (b, e), and SQ (c, f) at different temperatures, $z = 22 \text{ mm}$, and $Q_L = 0.5 \text{ mL min}^{-1}$.

deviations of 10% were obtained (see the parity plot in Figure 8a).

3.3. CFD Modeling and Validation. The numerical investigation was continued by coupling the species mass transport (eqs 11 and 12) to the fluid dynamic study (eqs 8 and 9) including the reaction rates (given in Table 2). The results obtained in the resolution of the CFD model in terms of the concentration of phenol and H_2O_2 at the channel exit at different liquid flow rates and reaction temperature have been compared with the experimental results obtained for the same cell geometry. Figure 8b represents the parity plot between the experimental and the CFD concentration. A similar dispersion of the data as before can be seen, with the calculated concentrations from the kinetic model, thus the CFD model proposed to simulate the behavior of monolithic reactors with interconnected channels can be considered valid. The experimental (in symbols) and CFD-predicted (in lines) concentration profiles are provided in Figure S6 of the SI. This validation also indicates that the imperfections of the 3D-printed monoliths during the manufacturing (see Figure 1c)

are not critical for the CFD simulation, when ideal geometries are used (Figure S2 of the SI).

With this CFD modeling, it is now possible to conduct a numerical investigation to gain an insight into the behavior of the monolithic reactors with different morphologies in terms of the external and internal mass transfer; this information along with the fluid dynamic study will enable us to understand the functioning of the interconnected channeled monoliths and to develop a prototype of an optimized 3D monolithic structure for the production of DHBZ.

3.4. Mass Transfer Analysis. Figure 9 represents the radial reactant concentration profiles at the half height of the reactor ($z = 22 \text{ mm}$) for the different channel geometries at three temperatures and the intermediate flow conditions ($Q_L = 0.5 \text{ mL min}^{-1}$). The concentration profiles provided from $r = 0$ to $r \sim 0.15 \text{ mm}$ correspond to the reactant concentration inside the catalytic wall and from $r \sim 0.15 \text{ mm}$ to $r \sim 0.6 \text{ mm}$ in the open channel. As expected by the kinetic reaction rates, the phenol and H_2O_2 concentrations are lower inside the TRG, then RAD, and finally SQ channels. The highest radial concentration gradient is observed for the RAD cell at $T =$

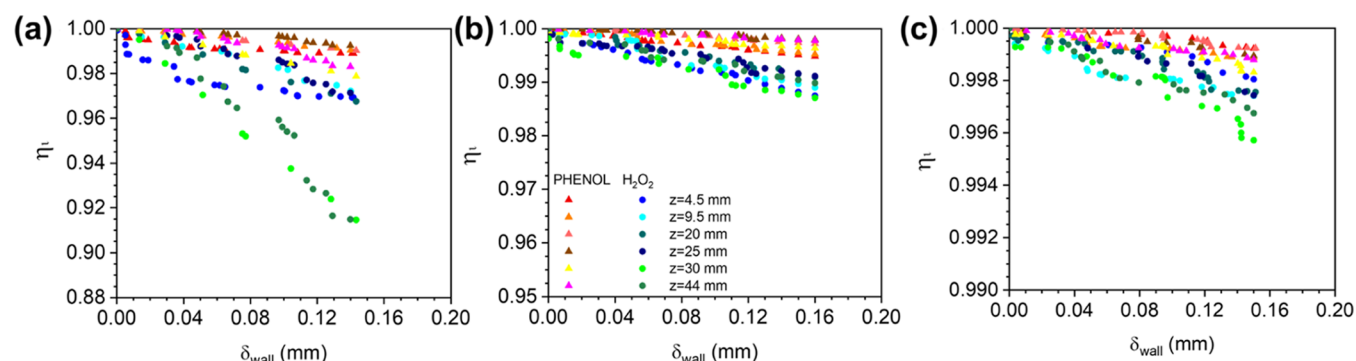


Figure 10. Evolution of the internal effectiveness factor (η_i) inside the catalytic wall for the different monolith morphologies: RAD (a), TRG (b), and SQ (c) morphologies at different reactor lengths ($z = 0\text{--}44\text{ mm}$), $T = 90\text{ }^{\circ}\text{C}$, and $Q_L = 0.25\text{ mL min}^{-1}$.

$90\text{ }^{\circ}\text{C}$ and for H_2O_2 (Figure 9a) because of the lower H_2O_2 diffusivity and the faster reaction rate at $90\text{ }^{\circ}\text{C}$. But still the gradient value is very low, less than 2% between the H_2O_2 concentration in the center and the wall surface. Therefore, the radial concentration profiles for all of the geometries can be considered flat in the open channel. Note that the TRG (Figure 9b,e) and SQ (Figure 9c,f) channels showed a flatter profile than RAD. The resulting radial profile is a trade-off between the mass transfer by radial diffusion of the reactants, favored in TRG channels by the induced oscillating flow, the convective flow, which is lower for the TRG since the flow slows down, and the reaction rate, lower in the SQ. These phenomena can explain the slight differences found in the TRG and SQ with respect to RAD channels. In any case, the effect of the external mass transfer in the chemical performance can be considered negligible for any channel geometry.

Regarding the reactant concentration profiles inside the catalytic wall, corresponding to $r = 0$ to $r \sim 0.15\text{ mm}$ shown in Figure 9, the decay in the phenol and, about all, H_2O_2 concentrations is more pronounced for the RAD (Figure 9a,d) than TRG (Figure 9b,e) and SQ (Figure 9c,f) geometries. For the former, there is a concentration gradient of 4% between the center of the channel and the external wall for H_2O_2 , which is reduced to less than 1% for phenol. This profile inside the rod of the monolith is a trade-off between the chemical reaction rate and the internal diffusion rate; the latter is expected to be more favored in the TRG due to the highest wall porosity. This effect can even compensate its wider wall thickness and the reaction rate that may be faster for SQ than RAD due to the higher reactant concentration profiles at the wall surface.

The analysis of the possible limitations due to internal diffusion has been carried out by calculating the internal effectiveness factor (η_i) as the ratio between the reaction rate inside the porous wall at different positions and the reaction rate at the wall surface along the monolith. Figure 10 shows the internal effectiveness factor for phenol and H_2O_2 as a function of the position inside the wall (this is at different z values) for the three geometries and at $90\text{ }^{\circ}\text{C}$ and $Q = 0.25\text{ mL min}^{-1}$ (the most favored conditions for the limitation of the internal diffusion). It can be seen how the internal effectiveness factor shows a certain dependence on the axial position (z), which is accentuated for H_2O_2 , since it possesses a lower molecular diffusivity in water and react faster than phenol. Because of the internal concentration profiles obtained (Figure 9), the RAD geometry shows the lowest η_i values, but considering that the internal effectiveness factor is lower than 0.95 only at $T = 90$

$^{\circ}\text{C}$, at the exit of the reaction ($z \geq 30\text{ mm}$) and the wall (after diffusing through the 83% of wall), it can be generally accepted that the chemical reaction is not limited by the internal diffusion of the reactants.

According to these results, the fabrication of nonconventional catalytic systems by additive manufacturing must be focused not only on the control of the reactor structure at the macroscale to induce fluctuation but also on preserving the accessibility to the active sites, as demonstrated by the numerical investigation carried out through the CFD simulation.

4. CONCLUSIONS

This study illustrates how the CFD tools combined with additive manufacturing pave the way for the design and optimization of nonconventional catalytic reactors with improved flow patterns that contribute to the acclaimed transformation of the chemical industry to shape a more sustainable and digital future.

In particular, monolithic catalysts with a TRG cell geometry robocast by superimposing three layers of filaments give rise to staggered interconnections between adjacent channels, while in other geometries, such as SQ and RAD cells, manufactured by superimposing two layers of filaments, the interconnections face in a two-by-two manner. As a result, the TRG geometry accounts for a higher macrochannel tortuosity that causes an oscillating flow inside the channel along with a transverse flow between adjacent parallel channels. In this way, the reactant mixture is increased and the exposure time of the reactants to the catalytic surface is prolonged (since the flow velocity is reduced by the collision of the fluid with the wall of the channels). All of these aspects increase both the reaction rates of the reactants and product selectivity.

In addition, the catalytic wall porosity is a concern in the additive manufacturing process. It must enable the appropriate access to the active sites without compromising the catalyst mechanical resistance.

■ ASSOCIATED CONTENT

Supporting Information

The Supporting Information is available free of charge at <https://pubs.acs.org/doi/10.1021/acs.iecr.1c03098>.

Details of the computer-designed geometries, mesh sensitivity analysis in COMSOL Multiphysics, videos of particle tracking, additional kinetic modeling, and computational data (PDF)

■ AUTHOR INFORMATION

Corresponding Author

Asuncion Quintanilla – Department of Chemical Engineering,
Universidad Autónoma de Madrid, 28049 Madrid, Spain;

orcid.org/0000-0002-7255-2547;

Email: asun.quintanilla@uam.es

Authors

Gonzalo Vega – Department of Chemical Engineering,
Universidad Autónoma de Madrid, 28049 Madrid, Spain

Pablo López – Department of Chemical Engineering,
Universidad Autónoma de Madrid, 28049 Madrid, Spain

Francesca García – Department of Chemical Engineering,
Universidad Autónoma de Madrid, 28049 Madrid, Spain

Enrique Madurga – Department of Chemical Engineering,
Universidad Autónoma de Madrid, 28049 Madrid, Spain

Manuel Belmonte – Institute of Ceramics and Glass (ICV-
CSIC), 28049 Madrid, Spain; orcid.org/0000-0001-
6668-6920

Jose A. Casas – Department of Chemical Engineering,
Universidad Autónoma de Madrid, 28049 Madrid, Spain

Complete contact information is available at:

<https://pubs.acs.org/10.1021/acs.iecr.1c03098>

Notes

The authors declare no competing financial interest.

■ ACKNOWLEDGMENTS

The authors thank the financial support by the Community of Madrid through the project S2018/EMT-4341 and the Government of Spain through the projects: PGC2018-095642-B-I00 and RTI2018-095052-B-I00 (MCIU/AEI/FEDER, UE). Also, G. Vega acknowledges the Universidad Autónoma de Madrid for the predoctoral contract.

■ REFERENCES

- (1) Foutch, G. L.; Johannes, A. H. Reactors in Process Engineering. In *Encyclopedia of Physical Science and Technology*; Academic Press Inc: CA, 2003; pp 23–43.
- (2) Reay, D.; Ramshaw, C.; Harvey, A. *Process Intensification: Engineering for Efficiency, Sustainability and Flexibility* Elsevier: Amsterdam, The Netherlands, 2008; Chapter 5, pp 103–186.
- (3) Magureanu, M.; Mandache, N. B.; Parvulescu, V. I.; Subrahmanyam, Ch.; Renken, A.; Kiwi-Minsker, L. Improved performance of non-thermal plasma reactor during decomposition of trichloroethylene: Optimization of the reactor geometry and introduction of catalytic electrode. *Appl. Catal., B* **2007**, *74*, 270.
- (4) Parra-Cabrera, C.; Achille, C.; Kuhn, S.; Ameloot, R. 3D printing in chemical engineering and catalytic technology: structured catalysts, mixers and reactors. *Chem. Soc. Rev.* **2018**, *47*, 209.
- (5) Zentel, K. M.; Fassbender, M.; Power, W.; Luintra, Q. A. 3D Printing as Chemical Reaction Engineering Booster. In *Advances in Polymer Reaction Engineering*; Academic Press: Cambridge, MA, 2020; Chapter 4, Vol. 56, p 97.
- (6) Lawson, S.; Rezaei, F.; Rownaghi, A. Additively-Manufactured Structure for Reactionary Processes. U.S. Patent US2020398456A12020.
- (7) Bogdan, E.; Michorczyk, P. 3D Printing in Heterogeneous Catalysis-The State of the Art. *Materials* **2020**, *13*, 4534.
- (8) Symes, M. D.; Kitson, P. J.; Yan, J.; Richmond, C. J.; Cooper, G. J. T.; Bowman, R. W.; Vilbrandt, T.; Cronin, L. Integrated 3D-printed reactionware for chemical synthesis and analysis. *Nat. Chem.* **2012**, *4*, 349.
- (9) Kitson, P. J.; Glatzel, S.; Chen, W.; Lin, C. G.; Song, Y. F.; Cronin, L. 3D printing of versatile reactionware for chemical synthesis. *Nat. Protoc.* **2016**, *11*, 920.
- (10) Hou, W.; Bubliauskas, A.; Kitson, P. J.; Francoi, J. P.; Powell-Davies, H.; Gutierrez, J. M. P.; Frei, P.; Manzano, J. S.; Cronin, L. Automatic Generation of 3D-Printed Reactionware for Chemical Synthesis Digitization using ChemSCAD. *ACS Cent. Sci.* **2021**, *7*, 212.
- (11) Kitson, P. J.; Rosnes, M. H.; Sans, V.; Dragone, V.; Cronin, L. Configurable 3D-Printed millifluidic and microfluidic 'lab on a chip' reactionware devices. *Lab Chip* **2012**, *12*, 3267.
- (12) Barone, S.; Braglia, M.; Gabbriellini, R.; Miceli, S.; Neri, P.; Paoli, A.; Rationale, A. V. Fabrication of fluidic reactors by a customized 3D printing process. *Procedia Struct. Integr.* **2018**, *12*, 113.
- (13) Laguna, O. H.; Lietor, P. F.; Iglesias Godino, F. J.; Corpas-Iglesias, F. A. A review on additive manufacturing and materials for catalytic applications: Milestones, key concepts, advances and perspectives. *Mater. Des.* **2021**, *208*, No. 109927.
- (14) Liu, G.; Zhang, X.; Chen, X.; He, Y.; Cheng, L.; Huo, M.; Yin, J.; Hao, F.; Chen, S.; Wang, P.; Yi, S.; Wan, L.; Mao, Z.; Chen, Z.; Wang, X.; Cao, Z.; Lu, J. Additive manufacturing of structural materials. *Mater. Sci. Eng., R* **2021**, *145*, No. 100596.
- (15) Stuecker, J. N.; Miller, J. E.; Ferrizz, R. E.; Mudd, J. E.; Cesarano, J. Advanced Support Structures for Enhanced Catalytic Activity. *Ind. Eng. Chem. Res.* **2004**, *43*, 51.
- (16) Ferrizz, R. M.; Stuecker, J. N.; Cesarano, J.; Miller, J. E. Monolithic supports with unique geometries and enhanced mass transfer. *Ind. Eng. Chem. Res.* **2005**, *44*, 302.
- (17) Li, Y.; Chen, S.; Cai, X.; Hong, J.; Wu, X.; Xu, J.; Zou, J.; Chen, B. H. Rational design and preparation of hierarchical monoliths through 3D printing for syngas methanation. *J. Mater. Chem. A* **2018**, *6*, 5695–5702.
- (18) Noyen, J.; Wilde, A.; Schroeve, M.; Mullens, S.; Luyten, J. Ceramic Processing Techniques for Catalyst Design: Formation, Properties, and Catalytic Example of ZSM-5 on 3-Dimensional Fiber Deposition Support Structures. *Int. J. Appl. Ceram. Technol.* **2012**, *9*, 902.
- (19) Quintanilla, A.; Casas, J. A.; Miranzo, P.; Osendi, M. I.; Belmonte, M. 3D-Printed Fe-Doped silicon carbide monolithic catalysts for wet peroxide oxidation processes. *Appl. Catal., B* **2018**, *235*, 246.
- (20) Salazar-Aguilar, A. D.; Quintanilla, A.; Vega-Díaz, S. M.; Casas, J. A.; Miranzo, P.; Osendi, M. I.; Belmonte, M. Iron-based metal-organic frameworks integrated into 3D printed ceramic architectures. *Open Ceram.* **2021**, *5*, No. 100047.
- (21) Davó-Quinóner, A.; Soroll-Rosario, D.; Bailón-García, E.; Lozano-Castelló, D.; Bueno-López, A. Improved asymmetrical honeycomb monolith catalyst prepared using a 3D printed template. *J. Hazard. Mater.* **2019**, *368*, 638.
- (22) Wei, Q.; Li, H.; Liu, G.; He, Y.; Wang, Y.; Tan, Y. E.; Wang, D.; Peng, X.; Yang, G.; Tsubaki, N. Metal 3D printing technology for functional integration of catalytic system. *Nat. Commun.* **2020**, *11*, No. 4098.
- (23) Tubío, C. R.; Azuaje, J.; Escalante, L.; Coelho, A.; Guitián, F.; Sotelo, E.; Gil, A. 3D printing of a heterogeneous copper-based catalyst. *J. Catal.* **2016**, *334*, 110.
- (24) Agueniou, F.; Vidal, H.; de Dios López, J.; Hernández-Garrido, J. C.; Cauqui, M. A.; Botana, F. J.; Calvino, J. J.; Galvita, V. V.; Gatica, J. M. 3D-printing of metallic honeycomb monoliths as a doorway to a new generation of catalytic devices: the Ni-based catalysts in methane dry reforming showcase. *Catal. Commun.* **2021**, *148*, No. 106181.
- (25) Kovacev, N.; Li, S.; Zeraati-Rezaei, S.; Hemida, H.; Tzolakis, A.; Essa, K. Effects of the internal structures of monolith ceramic substrates on thermal and hydraulic properties: additive manufacturing, numerical modelling and experimental testing. *Int. J. Adv. Manuf. Technol.* **2021**, *112*, 1115.
- (26) Jungreuthmayer, C.; Steppert, P.; Sekot, G.; Zankel, A.; Reingruber, H.; Zanghellini, Z.; Jungbauer, A. The 3D pore structure and fluid dynamics simulation of macroporous monoliths: High

permeability due to alternating channel width. *J. Chromatogr. A* **2015**, *1425*, 141.

(27) Vega, G.; Quintanilla, A.; Menendez, N.; Belmonte, M.; Casas, J. A. 3D-honeycomb monoliths with interconnected channels for the sustainable production of dihydroxybenzenes: towards the intensification of selective oxidation processes. *Chem. Eng. Process.* **2021**, *165*, 108437.

(28) Kashani-Shirazi, N.; Wloka, V.; Gerlinger, W.; Schmidt, A.; Heinen, K.; Kollenberg, W. Use of Shaped Bodies Having Catalytic Properties as Reactor Internals. U.S. Patent US20100222209 A12010.

(29) Gauze Packings – <https://www.sulzer.com/en/shared/products/gauze-packings> (accessed July 12, 2021).

(30) Hajimirzaee, S.; Doyle, A. M. 3D printed catalytic converters with enhanced activity for low-temperature methane oxidation in dual-fuel engines. *Fuel* **2020**, *274*, 117848.

(31) Chaparro-Garnica, C. Y.; Jordá-Faus, P.; Bailón-García, E.; Ocampo-Pérez, R.; Aguilar-Madera, C. G.; Davó-Quñonero, A.; Lozano-Castelló, D.; Bueno-López, A. Customizable Heterogeneous Catalysts: Nonchanneled Advanced Monolithic Supports Manufactured by 3D-Printing for Improved Active Phase Coating Performance. *ACS Appl. Mater. Interfaces* **2020**, *12*, 54573.

(32) Vega, G.; Quintanilla, A.; Belmonte, M.; Casas, J. A. Kinetic study of phenol hydroxylation by H₂O₂ in 3D Fe/SiC honeycomb monolithic reactors: enabling the sustainable production of dihydroxybenzenes. *Chem. Eng. J.* **2022**, *428*, 131128.

(33) Eisenberg, G. M. Colorimetric determination of hydrogen peroxide. *Ind. Eng. Chem., Anal. Ed.* **1943**, *15*, 327.